Thermal Science and Engineering Progress 77 (2026) 104837

Contents lists available at ScienceDirect

Thermal Science and Engineering Progress

journal homepage: www.elsevier.com/locate/tsep

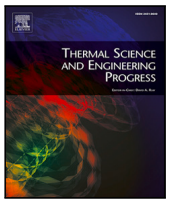

Numerical investigation of heat dissipation performance of immersion cooling for Li-ion batteries using fluids with different boiling points

Luca Reina [a,*], Javier Marco-Gimeno [b], Carlos Micó [b], Stefano Fontanesi [a], Antonio García [b]

[a] Engineering Department "Enzo Ferrari", University of Modena and Reggio Emilia, Via Vivarelli 10, Modena, 41125, Italy
[b] CMT - Clean Mobility and Thermofluids, Universitat Politècnica de València, Camino de Vera s/n, Valencia, 46022, Spain

ARTICLE INFO

Keywords:
Lithium-ion battery
Thermal runaway
Immersion cooling
Multiphase
Boiling
CFD

ABSTRACT

The growing use of Lithium-Ion Batteries (LIB) in high-demand applications underscores the need for advanced thermal management solutions to prevent Thermal Runaway (TR) and ensure operational safety. Although several numerical studies have demonstrated the high cooling efficiency of Immersion Cooling (IC) under normal operating conditions, the behavior of IC systems during abuse scenarios remains largely unexplored. To address this gap, this study presents a computational analysis of two IC strategies, single-phase and two-phase, using dielectric fluids with different boiling points. A detailed computational model was developed, integrating a TR mechanism and a multiphase boiling model. Simulation results revealed that both IC configurations enhance safety performance compared to more conventional cooling strategies since they require significantly higher heat input to trigger TR. The two-phase IC, using a low boiling point fluid, showed good performance at lower temperatures due to the heat transfer improved by evaporation. However, early vapor film formation near the TR onset temperature significantly reduces its heat dissipation capability. In contrast, the single-phase IC with a high boiling point fluid exhibits a good performance in a wider range of temperatures, delaying evaporation to temperatures reached only when TR takes place and reducing the influence of the vapor film formation. Following certain modeling assumptions, the methodology is able to highlight key differences between both strategies and their influence on heat dissipation, internal temperature distribution and TR evolution. Ultimately, conclusions highlight the strong potential of IC strategies in improving LIB safety under abuse conditions and support further investigation for real-world implementation.

1. Introduction

Due to urbanization, population growth, and an increasingly industrialized and energy-demanding world, the emissions of greenhouse and polluting gases are rising [1]. To address this issue, governments worldwide have been vigorously promoting the electrification of transport and energy storage systems [1–3]. Within this context, Lithium-Ion Batteries (LIBs) have emerged as a pivotal battery technology [4] due to their high energy density, extended cycle lifespan and relatively low environmental impact [1–3,5].

However, with the growing interest in large-format LIBs for automotive applications and mass production, safety has become a key concern [6,7]. Higher energy density corresponds to lower thermal stability [7]. Consequently, recent regulations are paying more attention to safety performance of LIBs under non-normal operating conditions [8]. Indeed, when exposed to abnormal circumstances such as mechanical damage, internal short-circuit, overcharging/over-discharging, or thermal abuse, the battery experiences abnormal heating, triggering several exothermic and self-sustaining decomposition reactions of its components [3,4]. It is widely accepted [9–11] that as the temperature rises to 70–90 °C, the Solid Electrolyte Interface (SEI) film begins to decompose, initiating the self-heating of the battery cell. Once the SEI is degraded, the lithium metal intercalated in the anode reacts with the electrolyte, generating additional heat. As the temperature continues to rise, the electrolyte starts to decompose, and the separator begins to shrink. When the separator collapses completely, a massive Internal Short Circuit (ISC) occurs, releasing a large amount of heat almost instantaneously and causing a rapid increase in battery cell temperature. Due to this temperature increase, the cathode active material decomposes, releasing oxygen, which further oxidizes the electrolyte and reacts with the anode active material, further increasing the battery cell temperature. During all this process, flammable gases such as H_2, CO, CH_4, C_2H_4, and C_2H_6 are produced, which may ignite and result in

* Corresponding author.
E-mail address: luca.reina@unimore.it (L. Reina).

https://doi.org/10.1016/j.tsep.2026.104837
Received 17 March 2026; Received in revised form 17 June 2026; Accepted 8 July 2026
Available online 22 July 2026

Nomenclature

c_p	Specific heat capacity, J kg^{-1} K^{-1}
T	Temperature, K
$\dot{Q}$	Volumetric heat source, W m^{-3}
H	Reaction enthalpy, J kg^{-1}
m	Reactant mass, kg
V	Battery cell volume, m^3
K	Reaction rate, s^{-1}
A	Pre-exponential factor, s^{-1}
E_a	Activation energy, J mol^{-1}
R	Universal gas constant, J mol^{-1} K^{-1}
c	Reactant normalized concentration, –
n_1, n_2	Reaction order exponents, –
G	Mechanism function, –
V	Volume, m^3
Sc^t	Turbulent Schmidt number, –
S_α	Phase source term, s^{-1}
t	Time, s
T_f	Near-wall fluid temperature, K
T_w	Wall temperature, K
T_{sat}	Saturation temperature, K
n_p	Prandtl number exponent, –
Pr	Prandtl number, –
C_{qw}	Empirical coefficient, –
g	Gravitational acceleration, m s^{-2}
h_{lat}	Latent heat, J kg^{-1}
C_{ew}	Model constant, –
q	Heat flux, W m^{-2}
ΔT	Excess temperature, K
S	Scale factor, –
K_1, K_2	Positive exponents, –
R^2	Coefficient of determination, –

Greek symbols

ρ	Density, kg m^{-3}
κ	Thermal conductivity, W m^{-1} K^{-1}
α	Volume fraction, –
μ_t	Turbulent dynamic viscosity, Pa s
μ	Dynamic viscosity, Pa s
σ	Surface tension, N m^{-1}
ϕ	Constant, N m^{-1}

Vectors

$\mathbf{u}$	Velocity, m s^{-1}
$\mathbf{u}_d$	Diffusive velocity, m s^{-1}

fire and explosion. This condition, known as Thermal Runaway (TR), must be carefully managed in order to prevent both its onset and its propagation to neighboring cells.

Effective Battery Thermal Management Systems (BTMSs) are essential for maximizing power and lifespan while mitigating the risk of TR by dissipating heat and maintaining optimal operating temperatures [9,12]. Traditional BTMSs primarily include forced air cooling, liquid cold plate, heat pipes and thermal insulation layers [4,9,12].

Emerging alternatives to these BTMSs involve the use of Phase-Change Materials (PCM) and direct liquid Immersion Cooling (IC) [4,9]. The former absorbs and releases heat during melting and solidification [9], preventing LIBs from overheating and ensuring they operate within the appropriate temperature range [4]. The latter, which submerges LIBs in a dielectric fluid, enhances the heat dissipation due to its ability to maintain temperature uniformity and ensure direct contact with the battery cells [4,9,12]. Additionally, dielectric fluids are often flame-retardant [9,12], aiding in the suppression of TR and improving safety. Depending on the properties of the dielectric fluid, IC can be single-phase or two-phase. In two-phase IC, the latent heat of vaporization associated with the phase transition between liquid and vapor enables higher heat transfer compared to the single-phase IC [9], but it also increases system complexity [12]. To date, these systems are far from being extensively implemented at an industrial scale due to challenges related to cost, lifespan, weight, and integration [12].

To evaluate the safety of LIBs and their BTMSs, manufacturers often perform series of safety tests. These "trial-and-error" experiments are labor-intensive and inefficient in terms of time, cost and the information they provide [6,7]. In this context, Computational Fluid Dynamics (CFD) and heat transfer simulations can play a crucial role, by enabling design testing in a virtual environment, thereby reducing the number of required experimental tests.

Various CFD studies on IC are available in the scientific literature [13–23], mostly focusing on evaluating the performance of this technology within the normal operating range of LIBs. The main outcome of these studies is the high cooling efficiency of IC compared to other cooling systems, particularly in maintaining lower operating temperatures and reducing temperature gradients across cells within a module. However, to the authors' knowledge, few works have investigated IC under abuse conditions. Liu et al. [4], for instance, conducted a CFD study comparing the effectiveness of PCM and IC in mitigating TR propagation within a battery module during a ISC event, highlighting the potential of IC in suppressing propagation.

In contrast, the majority of studies have experimentally investigated the role of IC under abuse conditions, both at the single-cell level [24,25] and within small battery modules [26,27], consistently demonstrating that IC can significantly mitigate and delay, or in some cases fully suppress TR. In particular, IC is shown to reduce the peak temperature and prolong the overall reaction duration, substantially reducing the severity and hazards of TR.

Guided by the insights from mentioned experimental studies, the present work develops a computational model of a LIB to investigate the cooling effectiveness of three BTMSs configurations under abuse conditions. Specifically, natural convection air cooling is compared with IC using two dielectric fluids with different boiling points, assessing the power and energy required to trigger TR in each case.

The aim of this study is to address the gap in the literature by providing a detailed CFD-based evaluation of IC under thermal abuse scenarios, an area still largely unexplored despite the demonstrated potential of this technology. Unlike previous studies, the effectiveness of different BTMS configurations is quantified in terms of the power and energy required to trigger TR. In addition, a systematic comparison of IC using dielectric fluids with different boiling points is presented, for which no dedicated comparative studies are currently available. This approach provides new insights into the role of fluid properties in mitigating TR and contributes to the understanding and optimization of safer battery thermal management strategies.

2. Model structure

The battery cell utilized in the present work is a cylindrical 18650 LIB with an outer diameter of 18.39±0.11 mm, an axial height of 65.0±0.15 mm, and total mass of 44.5±1.0 g. The external casing is made of nickel-plated steel. The cathode chemistry is NMC811 while the anode is composed of graphite. The cell operates within a voltage range of 2.5–4.2 V, has a rated capacity of 3.2 Ah, and a gravimetric energy density of 252 Wh/kg.

The two dielectric fluids used in this study are 3M™ Novec™ 649 Engineered Fluid and 3M™ Fluorinert™ Electronic Liquid FC-43. Both

Table 1
Physical properties of the two fluids considered in this study.

Properties	Novec 649	FC-43
Boiling temperature, °C	49	174
Molecular weight, g mol^{-1}	316	670
Heat of formation, J kg^{-1}	−88000	−70000
Density, kg m^{-3}	1674.4−2.904·T	1913−2.18·T
Dynamic viscosity, Pa s	Fig. 1(a)	Fig. 1(b)
Specific heat, J kg^{-1} K^{-1}	1091.9 + 0.3419·T + 0.0039·T^2	1014 + 1.554·T
Thermal cond., W m^{-1} K^{-1}	0.063403−0.000188·T	0.067−0.00007·T
Surface tension, N m^{-1}	0.0108	0.016

Where temperature T is expressed in °C.

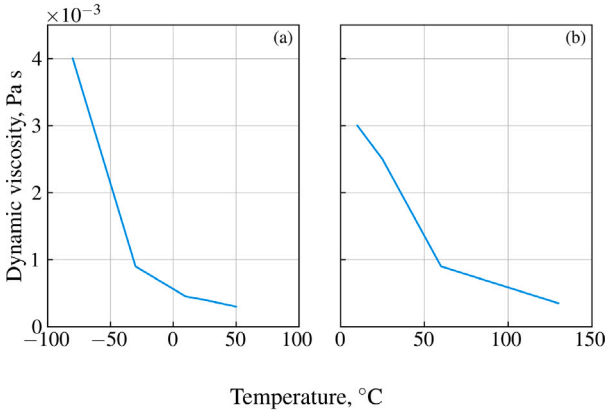

Fig. 1. Dynamic viscosity of 3M™ Novec™ 649 Engineered Fluid (a) and 3M™ Fluorinert™ Electronic Liquid FC-43 (b).

are advanced heat transfer fluids that are thermally and chemically stable, non-flammable, and exhibit low toxicity. Their key thermo-physical properties are summarized in Table 1 [28,29].

A computational model was developed using the commercial software Simcenter STAR-CCM+, licensed by Siemens DISW [30]. The TR model accounts solely for the heat generated during the degradation of internal components, excluding secondary phenomena such as venting, combustion, or particle ejection. This simplification is adopted to reduce computational cost, considering that the dominant heat generation is associated with the TR process itself, whereas the excluded phenomena become more significant when predicting TR propagation [1]. The main setup and sub-models are described in the following sections.

2.1. Thermal runaway model

A TR model aims to replicate the heat generation resulting from the degradation of internal components of a LIB under thermal abuse conditions. Among the modeling strategies found in the literature, a commonly used method involves fitting the heat generation rate to experimental data obtained from Accelerating Rate Calorimetry (ARC) tests [31]. While computationally efficient, this approach relies heavily on empirical measurements, which may not always be accessible or representative of real conditions.

In this work, a chemical kinetic model is adopted to simulate the heat released by the main decomposition reactions of the LIB. These models are capable of accurately capturing heat generation evolution under a variety of operating conditions. However, they are computationally more expensive and require a higher level of modeling complexity. One of the first TR kinetic models was proposed by Hatchard et al. [32] in 2001 and most current models are based on their work, including [6–8,33–35]. These models cover different LIB chemistries (e.g. $LiCO_2$ and $Li(Ni_xMn_yCo_z)O_2$), varying levels of detail (in terms of the number of reactions), and different dimensional frameworks (ranging from 0D to 3D). However, compared to the previous approach, they are more computationally expensive, as they introduce an ODE or a system of ODEs for each reaction that needs to be solved.

In all these models, the battery is treated as a single-component solid with volume-averaged properties. Within this solid domain, heat transfer is primarily governed by conduction, which can be described by the following equation:

$$\rho c_p \frac{\partial T}{\partial t} = \nabla \cdot (\kappa \nabla T) + \dot{Q} \tag{1}$$

where ρ is the material density, c_p is the specific heat capacity, T is the temperature, κ is the thermal conductivity, and $\dot{Q}$ is the volumetric heat source term.

The TR model is then coupled to the heat transfer model through the source term $\dot{Q} = \sum \dot{Q}_i$, which represents the cumulative heat release associated with the ith degradation reaction.

For each chemical reaction, the heat generation is calculated as:

$$\dot{Q}_i = \frac{m_i}{V} \cdot H_i \cdot K_i \tag{2}$$

where m_i is the reactant mass, V is the battery cell volume, H_i is the reaction enthalpy, and K_i is the reaction rate. While the reaction enthalpy and the reactant mass are constant values determined by the material and component type, the reaction rate is time-dependent and typically follows an Arrhenius-type expression:

$$K_i = A_i \cdot \exp\left(-\frac{E_{a,i}}{RT}\right) \cdot c_i^{n_{i,1}} \cdot (1 - c_i)^{n_{i,2}} \cdot G_i \tag{3}$$

$$c_i = c_{i,0} - \int K_i \, dt \tag{4}$$

where A_i is the pre-exponential factor, $E_{a,i}$ is the activation energy, R is the universal gas constant, c_i is the reactant normalized concentration and $c_{i,0}$ its initial value, $n_{i,1}$ and $n_{i,2}$ are reaction order exponents, and G_i is the mechanism function. The combination of the pre-exponential factor, activation energy and reaction enthalpy is commonly referred to as the thermal triplet, which can be experimentally determined through curve-fitting methods (e.g. Kissinger's equation [36]) applied to Differential Scanning Calorimetry (DSC), Thermal Gravimetric Analysis (TGA), or Differential Thermal Analysis (DTA) tests [8].

As previously mentioned, each TR mechanism exhibits a different level of detail, depending on the number of reactions included. In a previous comparative study [37], five mechanisms [6–8,33,34] were evaluated to assess their performance in predicting battery TR evolution. The results showed that, for NMC chemistry cathode, the variability in the decomposition temperature range was significantly lower compared to other chemistries. Based on these findings, the present work adopts the TR mechanism proposed by Ren et al. [7], to which a modified version of the electrolyte evaporation reaction from Kriston et al. [8] has been incorporated.

The adopted mechanism includes 6+1 reactions: (1) decomposition of the solid electrolyte interface layer (SEI); (2) reaction between the anode active material and the electrolyte (An); (3) reaction between anode active material and the binder (An-B); (4) decomposition of the cathode active material (Cat); (5) reaction between the oxygen released

Table 2
Parameters for the modified TR mechanism.

Reaction	i	A_i	$E_{a,i}$	$n_{i,1}$	$n_{i,2}$	H_i	g_i
		s^{-1}	kJ mol^{-1}	–	–	J g^{-1}	–
SEI decomp	SEI	6.3623×10^{9}	109.60	5.5	0	578.7	1
An and Ele	An	5.1510×10^{17}	200.77	1	0	253.2	1
An and Bin	An-B	4.9679×10^{15}	195.49	1	0	108.5	1
Cat decomp	Cat	5.3481×10^{5}	109.34	1.5	0	434.0	1
Cat and Bin	Cat-B	6.5429×10^{13}	177.85	2	0	452.1	1
Cat and An	Cat-An	2.4262×10^{13}	162.01	1	0	560.6	1
Ele evap	Ele	2.8990×10^{7}	95.14	1	0	−150.0	1

Table 3
Mass balance ODEs for the TR modified mechanism.

	dc/dt	c_0
SEI	$-R_{SEI}$	1
Anode	$-R_{An} - R_{CatAn}$	1
Binder	$-\frac{\gamma}{\gamma+1} R_{An-B} - R_{Cat-B}$	1
Cathode	$-R_{Cat}$	1
Electrolyte	$-R_{Ele}$	1

Where $\gamma = 3.4/6$ is the mass ratio of binder in the anode and in the cathode.

from cathode decomposition and the anode active material (Cat-An); (6) reaction between the oxygen released from cathode decomposition and the binder (Cat-B); (7) evaporation of the electrolyte (Ele). The parameter values for each reaction are provided in Tables 2 and 3.

2.2. Multiphase and boiling phase-change models

As described in Section 1, depending on the dielectric fluid properties, IC can be single-phase or two-phase. In the latter case, the latent heat associated with the phase change is utilized to enhance the cooling of the LIB. Modeling this phenomenon thus requires a multiphase model capable of accounting for phase transition.

The two main Eulerian-based approaches are the Eulerian Multiphase (EMP) model and the Mixture Multiphase (MMP) model. The major difference between them lies in the treatment of the secondary phase. The EMP model solves separate transport equations for mass, momentum, and energy for each individual phase, allowing detailed tracking of interphase dynamics. Oppositely, the MMP model solves these equations for the mixture of phases as a whole, and uses an additional equation for the volume fraction transport of each phase.

Since the scope of this the work is to evaluate the effectiveness of the cooling system and specifically the overall heat removed from the LIB, the MMP model is adopted. This approach captures the relevant macroscopic effects while reducing both model complexity and computational cost. In particular, the Volume of Fluid (VOF) model is used. It is a subtype of the MMP family that allows for sharp interface tracking between immiscible phases. The phases distribution and the position of the interface within the computational domain is described by the phase volume fraction. For phase i the volume fraction is defined as $\alpha_i = V_i/V$, where V_i is the volume occupied by phase i and V is the total volume of the computational cell. The properties of the mixture are calculated as a volume-fraction-weighted average of the properties of the individual phases. The distribution of phase i is determined by the volume fraction transport equation:

$$\frac{\partial \alpha_i}{\partial t} + \nabla \cdot (\alpha_i \mathbf{u}) + \nabla \cdot (\alpha_i \mathbf{u}_{d,i}) = \nabla \cdot \left(\frac{\mu_t}{\rho Sc^t} \nabla \alpha_i \right) + S_{\alpha_i} \tag{5}$$

where ρ is the density of the mixture, $\mathbf{u}$ is the mixture velocity, $\mathbf{u}_{d,i}$ is the diffusive velocity of phase i, μ_t is the turbulent dynamic viscosity, Sc^t is the turbulent Schmidt number, and S_{α_i} is the source term for phase i. The latter accounts for phenomena such as evaporation or condensation, and therefore the model requires to be coupled with a phase-change model.

In IC applications, the primary phase is liquid (l), while the secondary phase is vapor (v). Consequently, the relevant phase-change mechanism is boiling. The models available in the software are the Rohsenow boiling model and the transition boiling model.

The Rohsenow boiling model applies the empirical correlation proposed by Rohsenow [38] to calculate the heat flux due to boiling:

$$q_{bw} = \mu_l h_{lat} \sqrt{\frac{g(\rho_l - \rho_v)}{\sigma}} \left(\frac{c_{p_l}(T_w - T_{sat})}{C_{qw} h_{lat} {Pr_l}^{n_p}} \right)^{3.03} \tag{6}$$

where μ is the dynamic viscosity, h_{lat} is the latent heat of vaporization, g is the gravitational acceleration, σ is the surface tension at the liquid–vapor interface, T_w is the wall temperature, T_{sat} is the saturation temperature, C_{qw} is an empirical coefficient that depends on the fluid–surface combination, Pr is the Prandtl number, and n_p is its exponent.

The vapor mass generation rate over the area covered by nucleation sites is then computed as:

$$\dot{m}_{ew} = \frac{C_{ew} q_{bw}}{h_{lat}} \tag{7}$$

where C_{ew} is a model constant that defines the fraction of the boiling heat flux contributing to vapor bubble generation.

Eq. (6) does not explicitly include the fluid temperature, meaning that heat is introduced into the domain independently of the local fluid temperature. Therefore, if this correlation is applied outside its natural range of applicability (i.e. nucleate boiling), the model may lead to unrealistically high heat flux predictions. To prevent this issue, the software includes a corrective factor for q_{bw}, which considers the local fluid temperature near the heated wall T_f [39]:

$$\max \left[0, \min \left(\frac{T_w - T_f}{T_w - T_{sat}}, 1 \right) \right] \tag{8}$$

When $T_f < T_{sat}$, the Rohsenow correlation is applied without modification, whereas when $T_f > T_w$ the boiling heat flux is set to zero. For fluid temperatures between the saturation and the wall temperatures, only a fraction of the heat flux predicted by the correlation is applied.

Referring to Fig. 2, when the wall temperature becomes sufficiently high, a continuous vapor layer forms between the wall and the liquid, preventing direct contact. In this condition, evaporation occurs at the vapor–liquid interface, and the resulting vapor film acts as an insulating layer, significantly reducing the heat transfer rate. However, as the temperature continues to rise, radiative heat transfer through the vapor film becomes increasingly significant, partially compensating for the insulating effect. This regime is known as film boiling. The intermediate region between nucleate boiling and film boiling is referred to as transition boiling, where both regimes coexist simultaneously.

To better account for this reduction in the heat transfer rate at sufficiently high wall temperatures, the transition boiling model can be employed. This model extends the capabilities of the previous formulation by capturing the non-monotonic behavior of the boiling curve during the transition regime. Specifically, the boiling heat flux is defined

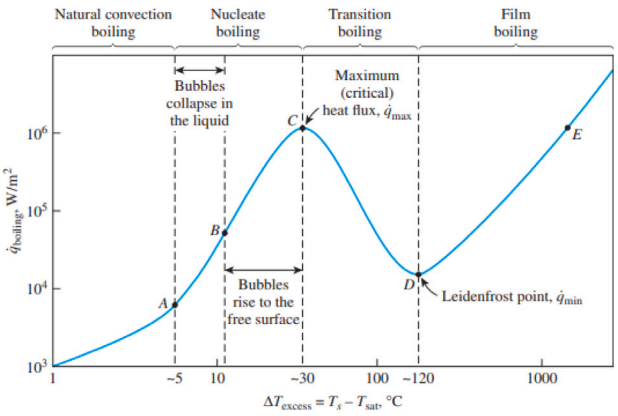

Fig. 2. Typical boiling curve for water at 1 atm [40].

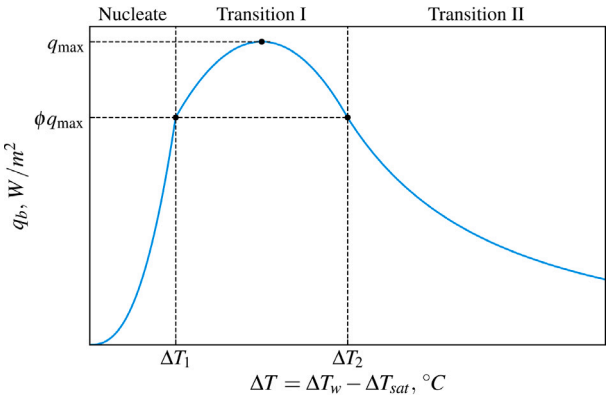

Fig. 3. Conceptual sketch of transition boiling model regimes.

as a piecewise continuous function, with each segment representing a distinct boiling regime (Fig. 3):

$$q_b(\Delta T) = \begin{cases} q_{max} S\phi \left(\frac{\Delta T}{\Delta T_1}\right)^{K_1} & 0 \le \Delta T \le \Delta T_1 \\ q_{max} S \left[1 - 4(1-\phi)\left(\frac{\Delta T - \Delta T_{max}}{\Delta T_2 - \Delta T_1}\right)^2\right] & \Delta T_1 \le \Delta T \le \Delta T_2 \\ q_{max} S\phi \left(\frac{\Delta T}{\Delta T_2}\right)^{-K_2} & \Delta T_2 \le \Delta T \end{cases} \quad (9)$$

where $\Delta T = T_w - T_{sat}$ is the wall superheat, q_{max} is the maximum boiling heat flux, ΔT_1 and ΔT_2 are the characteristic wall superheats defining the transition between regimes, K_1 and K_2 are positive exponents, S is a scale factor, and ϕ is a fixed constant equal to 0.75. The five parameters q_{max}, ΔT_1, ΔT_2, K_1, and K_2 must be calibrated against experimental data.

As an initial approach, the authors opted to rely on experimental data available in the scientific literature for the selected dielectric fluids, with the development of a dedicated experimental setup planned for future work. Specifically, the experimental results reported by Falsetti et al. [41] were used to calibrate the parameters of the Rohsenow boiling model, through the development of a 3D-CFD model replicating their experimental setup. The computational domain consisted of a heated horizontal surface in contact with a liquid pool, replicating the characteristics of the test section described in the reference work. Appropriate boundary conditions were applied to match the thermal and flow conditions reported in the experiments. The outcome of this calibration and the corresponding parameter values are presented in Fig. 4 and Table 4, respectively.

The choice of this specific model was primarily driven by the availability of compatible experimental data for calibration. Indeed, the majority of the experimental data available in the literature focus on

Table 4
Rohsenow boiling model parameters.

Parameter	Value
C_{qw}	0.012
n_p	1.73
Sc^t	0.9
C_{ew}	0.1

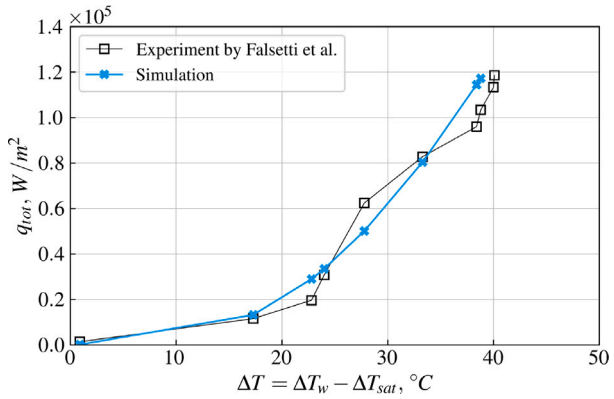

Fig. 4. Rohsenow boiling model calibration outcome.

the early stages of boiling, as the transition boiling regime has limited practical relevance because of its low heat transfer efficiency. Consequently, the available data provide a more direct basis for calibrating the Rohsenow model. However, as described above, the software implementation of the Rohsenow model includes a local-temperature correction of the boiling heat flux. Therefore, although the adopted formulation is not meant to exactly reproduce transition boiling, it differs from the original correlation and prevents an unconstrained increase of the boiling source term under high-temperature near-wall conditions.

To assess the impact of this modeling simplification, a comparative study between the Rohsenow and the transition boiling models was conducted. For this purpose, experimental data reported by [42] were used, as they cover all boiling regimes for the 3M™ Fluorinert™ FC-72 dielectric fluid.

The results of this comparative study are shown in Fig. 5, where the influence of the corrective factor for the Rohsenow model is highlighted. Although the transition model showed better accuracy in absolute terms, the corrected Rohsenow model effectively reproduced the general trend of the experimental data, providing a sufficiently accurate representation for the purposes of this study.

While experimental data for Novec 649 fluid are available in the scientific literature, equivalent data for FC-43 under comparable conditions are not readily available. Therefore, the boiling curve calibrated for Novec 649 was also adopted for FC-43 as an approximation, while fully acknowledging the differences in thermophysical properties between the two fluids. Although this represents a significant assumption, its impact is considered limited, as the primarily focus of this work is not to quantify the absolute heat removal performance, but rather to investigate the influence of boiling point on the thermal response and TR mitigation capability of the IC strategies.

2.3. Geometry and boundary conditions

A schematic of the computational domain and the corresponding mesh is presented in Fig. 6. The 18650 LIB cell is positioned inside a cylindrical canister, held in place by a dedicated support. Depending on the simulation setup, the canister is filled with either air or a dielectric fluid. This particular geometry was selected to maintain

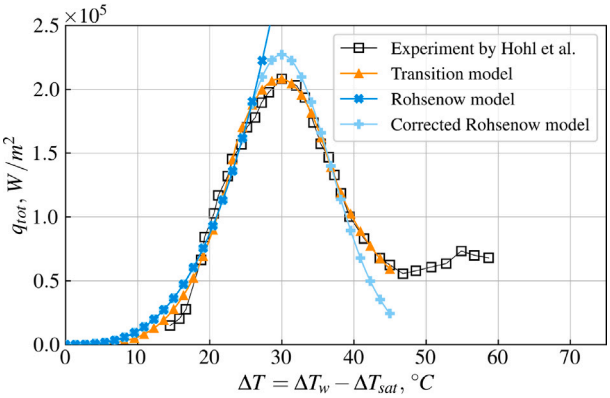

Fig. 5. Comparative study between the transition, Rohsenow, and corrected Rohsenow boiling model.

consistency with previous experimental studies, which served as basis for TR sub-model validation.

Leveraging the symmetry of the geometry, the computational domain is modeled as a two-dimensional axisymmetric section of the full geometry, significantly reducing computational cost. The mesh consists of approximately 3490 polyhedral elements, with a target surface size of 2.5 mm, a minimum surface size of 1 mm and a surface growth rate of 1.05. An all-y^+ wall treatment was adopted, and therefore the boundary-layer along solid walls was meshed accordingly using two prism layers with a stretching factor of 1.5 and a total thickness of 0.8 mm. Thin components, such as the LIB can, were discretized using at least two elements across their thickness to ensure adequate resolution.

The mesh was selected based on a mesh independence study, which confirmed that further refinement produced negligible variations in key simulation results. Moreover, excessive mesh refinement near hot walls was found to negatively affect the accuracy of phase-change predictions. In particular, the first near-wall cell tends to become rapidly saturated with vapor in finely resolved meshes, leading to an overestimation of vapor accumulation and premature suppression of heat transfer due to the loss of liquid contact. The adopted mesh represents a compromise that ensures numerical stability and physical fidelity of the boiling and heat transfer processes.

The computational domain is composed of three distinct regions: fluid, battery cell, and solids. Each region is assigned a dedicated continuum, in which specific physics sub-models are defined. While the boiling model is natively integrated into the software and applied to the fluid region, the TR model is not included by default. Therefore, it was implemented using the User Coding functionality of the software, which allows for custom model development through C-based coding, and then applied to the battery cell region.

The battery cell is artificially heated by applying a specific heat source to its region. A schematic representation of the heating procedure is shown in Fig. 7, where the specific heating power is increased in steps of 35 W kg^{-1}.

The k-ω SST turbulence model is used, as it combines the advantages of the k-ω formulation in the near-wall region with those of the k-ϵ formulation in the far-from-wall region.

The physical properties of the battery cell are listed in Table 5.

3. Results and discussion

Three simulations were performed using the computational setup described in Section 2, varying only the cooling configuration to allow for a direct performance comparison.

A commonly adopted criterion to identify the onset of TR is based on the temperature rise rate exceeding an empirical threshold of 10 °C/min [44]. This criterion is widely used in experimental studies, particularly under conventional abuse-test conditions. In the simulations performed, however, this threshold was reached only in the air-cooled case, whereas it was not exceeded in the two IC configurations. Maximum temperature rise rates of 8.3 °C/min and 7.1 °C/min were observed for the low- and high-boiling point fluid cases, respectively. Nevertheless, degradation reactions and a subsequent steep temperature increase still occurred. Therefore, to ensure a consistent comparison across all cooling strategies, two additional indicators were introduced:

- the concentration of the SEI decomposition reaction dropping below 0.98, used to identify the onset of decomposition reactions
- the temperature increase between two consecutive timesteps exceeding 10%, used to detect the beginning of the rapid thermal acceleration

Table 5
LIB physical properties.

Parameter	Value	Ref.
Density, kg m^{-3}	2580	[43]
Specific heat, J kg^{-1} K^{-1}	930	[43]
Thermal conductivity, W m^{-1} K^{-1}	3.4, 28, 28[a]	[43]

[a] In radial, circumferential and axial directions.

A global comparison of the three cooling strategies is first presented based on the last value of power applied to the LIB, in Fig. 8(a), and on the total energy provided, in Fig. 8(b). The results reveal a clear hierarchy in cooling effectiveness. The air-cooled configuration exhibits the least efficient thermal management, requiring the least power and energy input to trigger TR. This is due to its limited heat removal capabilities driven only by natural convection and radiation at the cell surface.

Conversely, the IC configurations exhibit markedly enhanced performance, requiring significantly higher power and energy input to reach TR conditions. Among them, the high boiling point configuration demonstrates the most robust thermal management, sustaining heating rates nearly an order of magnitude greater before the onset of the rapid thermal acceleration. This improvement stems from the superior heat transfer capabilities of the dielectric fluid and its elevated boiling point, which together extend the stable thermal operating window and delay the transition to unstable thermal behavior. The low boiling point configuration, with a boiling point of 49 °C, also performs significantly better than air cooling. As shown in Fig. 8, it requires more power and heat to initiate decomposition reactions compared to the high boiling point case, due to the initially higher heat removal efficiency of the boiling mechanism. However, the low boiling point limits the effectiveness of the system, leading to an earlier saturation of the boiling regime and the formation of dry-out zones on the battery surface, which reduce its ability to absorb additional heat. On the other hand, the high boiling point configuration, with a boiling point of 174 °C, postpones the onset of boiling while still maintaining efficient heat removal at elevated temperatures, preventing early dry-out during the initial stages of thermal abuse.

As discussed in Section 2.2, boiling is modeled using the Rohsenow correlation, which may overestimate heat transfer when operating near the limits of its natural applicability range, although the implementation used in the software constrains the values to remain within a physically reasonable range [39]. According to Eq. (7), the heat flux is directly proportional to the mass of vapor generated and therefore plays a pivotal role in determining both the onset and progression of dry-out phenomena.

The generation and transport of vapor within the IC configurations are crucial for overall heat removal. As shown in Fig. 9, once boiling conditions are reached, vapor bubbles begin to form on the

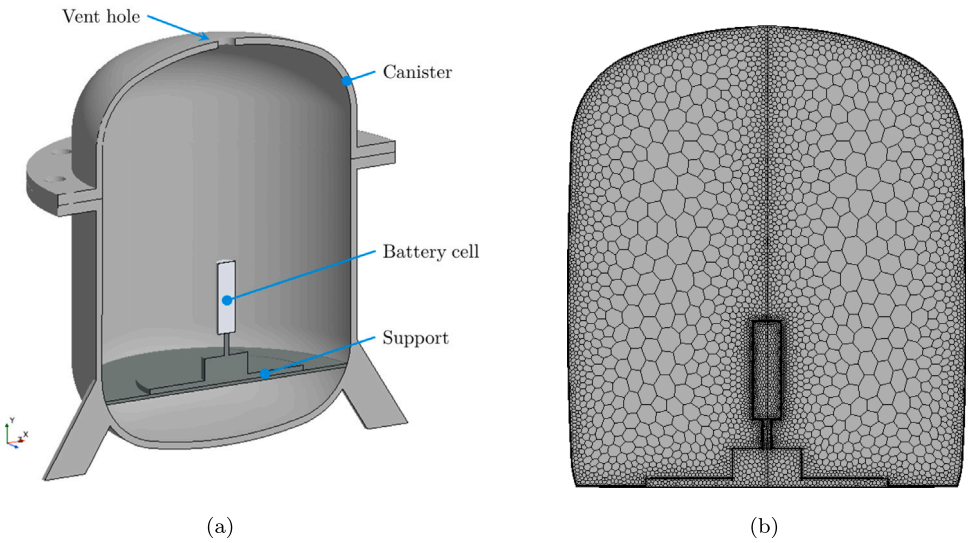

Fig. 6. Middle section of the model geometry (a) and computational grid (b).

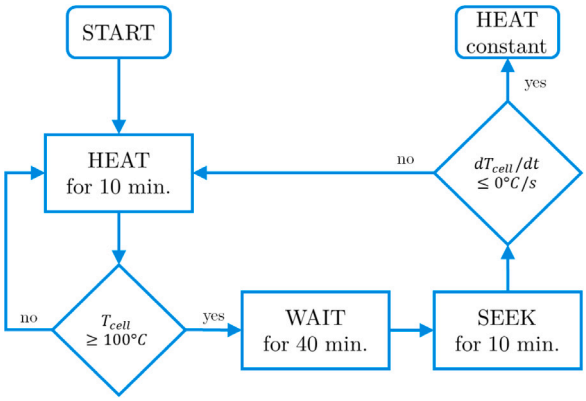

Fig. 7. Schematic representation of the heating procedure.

top and bottom surfaces of the battery. As heating progresses, the surface temperature continues to rise, intensifying vapor production and accelerating the nucleation process. This results in the progressive accumulation of vapor that eventually forms a continuous insulating layer over these surfaces, inhibiting direct contact between the fluid and the battery casing and drastically reducing the local heat transfer efficiency. This behavior rapidly extends to the lateral surface of the battery, causing widespread dry-out along the entire battery surface. The consequent degradation in cooling performance, combined with the heating procedure input, accelerates the progression toward TR. Upon rapid temperature-rise onset, a significant fraction of the fluid within the canister vaporizes, considerably reducing liquid volume.

Although vapor generation dynamics are qualitatively similar for both fluids, their temporal evolution differs significantly. In the low boiling point scenario, the boiling temperature is significantly lower than the typical TR trigger temperature and therefore by the time the battery approaches critical temperatures, the boiling regime is already near saturation. In contrast, in the high boiling point case, the boiling temperature exceeds the onset temperature of decomposition reactions. This improves heat transfer when it is most needed, slowing down the progression of degradation and resulting in a more temporally limited boiling process.

Further insight into thermal behavior is provided by the average temperature evolution of both the jellyroll and its casing, as shown in Fig. 10. In the air-cooled simulation, the cell exhibits a nearly uniform temperature increase until the onset of TR, which occurs at approximately 230 °C followed by a spike exceeding 550 °C. The temperature difference between the jellyroll and the external can remains relatively small, indicating poor heat transfer and internal thermal uniformity, both of which facilitate the rapid and uncontrolled propagation of the TR. In contrast, the IC configurations maintain a significantly lower jellyroll temperature throughout the simulation, effectively delaying the onset and reducing the severity of TR. Peak temperatures for the low and high boiling point configurations are approximately 200 °C and 350 °C, respectively.

Notably, a pronounced radial temperature gradient develops within the jellyroll, mainly due to the combined effects of efficient boundary heat removal driven by phase change and the low radial thermal conductivity. At the onset of TR, temperature fields reveal that only the inner core of the jellyroll reaches critical temperatures, while the outer layers remain considerably cooler, as depicted in Fig. 11. This spatial non-uniformity helps mitigate the severity of TR, as the energy release is localized and peak temperatures remain lower. Consequently, the reaction front remains confined to the core and does not propagate uniformly throughout the entire cell volume, as reflected by the more gradual temperature peak slope compared to the air-cooled scenario.

Fig. 10 also highlights, with vertical dashed lines, the time instants when the two indicators used to define the onset of reactions and temperature-rise are met. The initiation of decomposition reactions is strongly influenced by the heating rate experienced by the LIB [37]. Since the heating procedure is identical for all simulations, and the air-cooled configuration is the least effective in removing heat, it results in the highest heating rate and an average trigger temperature of approximately 130 °C. Conversely, the IC configurations show lower heating rates due to more efficient heat removal, leading to average trigger temperatures of approximately 92.5 °C and 104 °C for the low and high boiling point configurations, respectively.

The time at which the steep temperature rise occurs depends on the temperature evolution between the onset of decomposition reactions and this critical point. According to Eq. (3), the reaction rate is temperature-dependent, highlighting the importance of the cooling system in modulating reaction kinetics. In the low boiling point case, early boiling maintains lower average temperatures and establishes a strong thermal gradient within the jellyroll. This enables the core to reach temperatures sufficient to initiate self-sustaining reactions, while the cooler outer layers suppress outward propagation. This behavior is clearly illustrated in Fig. 12(b), which shows the dimensionless concentration profiles of the reactants. Although the initial reactant

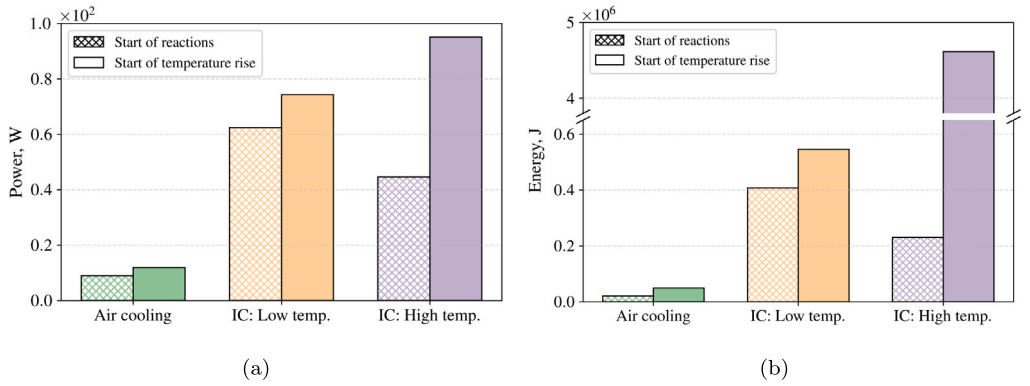

Fig. 8. Comparison of the power (a) and energy (b) required to trigger TR for different cooling configurations.

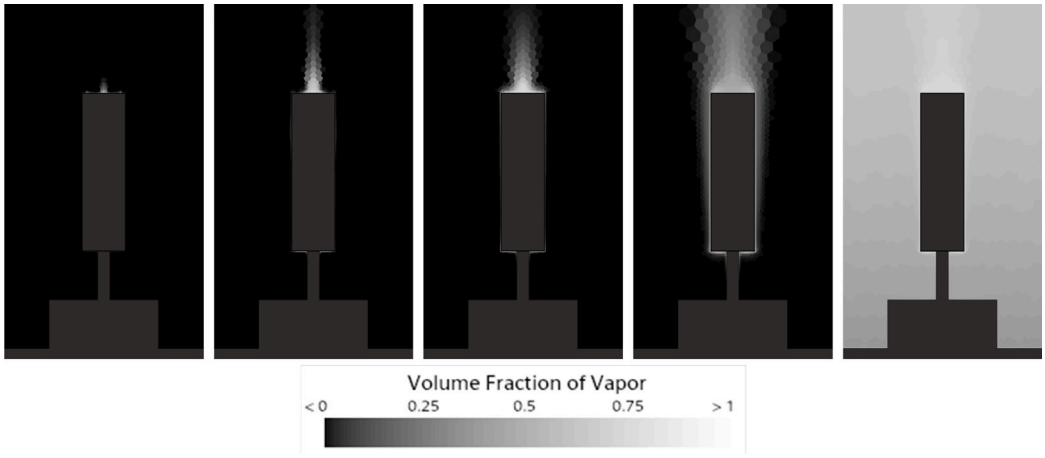

Fig. 9. Simulated temporal evolution of vapor volume fraction for the low boiling point fluid configuration.

consumption is similar to that of the air-cooled case in Fig. 12(a), the internal temperature gradient inhibits rapid reaction propagation, suppressing the evolution of TR. However, since the reactants are not fully depleted, a further increase in temperature could eventually trigger a subsequent onset of reactions. In the high boiling point configuration, boiling begins at a higher temperature, resulting in overall higher cell temperatures compared to the low boiling point case. Nonetheless, the superior heat removal capability of the IC system delays the onset of self-sustaining reactions. As shown in Fig. 12(c), the reactant consumption is slower and more gradual. When temperatures become sufficiently high, the system can no longer suppress TR, and reactions proceed until near-complete reactants depletion. By that time, however, a substantial portion of the energy has already been dissipated through phase change and most of the reactants have been consumed, explaining why the resulting temperature increase remains below 100 °C.

Despite the previously discussed model limitations, it is important to note that all the IC configurations assume a conservative pool boiling conditions with a stagnant liquid domain surrounding the cell. This setup is useful for isolating the thermal phenomena and evaluating the baseline performance of each cooling strategy. However, practical IC systems typically employ flow boiling, where the dielectric fluid is actively circulated around the cell surface. Flow boiling significantly enhances heat removal through forced convection, continuously refreshing the liquid interface and facilitating vapor removal. This dynamic condition delays vapor accumulation and dry-out onset, sustaining nucleate boiling for longer durations, increasing the critical heat flux [40] and maintaining lower cell surface temperatures.

4. Conclusions

The primary objective of this work was to evaluate the cooling performance of different BTMS configurations under abuse conditions, with the specific aim of quantifying their capability to mitigate TR. In addition to conventional assessments based solely on temperature evolution after TR onset, the cooling performance was also evaluated in terms of the power and energy required to trigger TR, enabling a direct and physically meaningful comparison among the different cooling strategies.

While experimental studies have clearly demonstrated the macroscopic effectiveness of IC in mitigating TR, the present numerical investigation provides complementary insights into the heat transfer mechanisms governing TR initiation under IC conditions.

To enable this analysis, a detailed computational model was developed, incorporating a user-defined TR model and a multiphase boiling model. The TR model includes 6+1 decomposition reactions, calibrated in a previous study, while for the boiling model the Rohsenow correlation was adopted, primarily due to the availability of experimental data compatible with its calibration for the selected dielectric fluids. The LIB was positioned inside a canister filled with either air or dielectric fluid and subjected to heating through a custom-defined procedure.

Among the tested configurations, the air-cooled case proved to be the least effective in mitigating or delaying TR. Due to its limited heat removal capability, TR was triggered at relatively low power and energy inputs, with a widespread and uniform decomposition of battery materials resulting in an abrupt temperature spike.

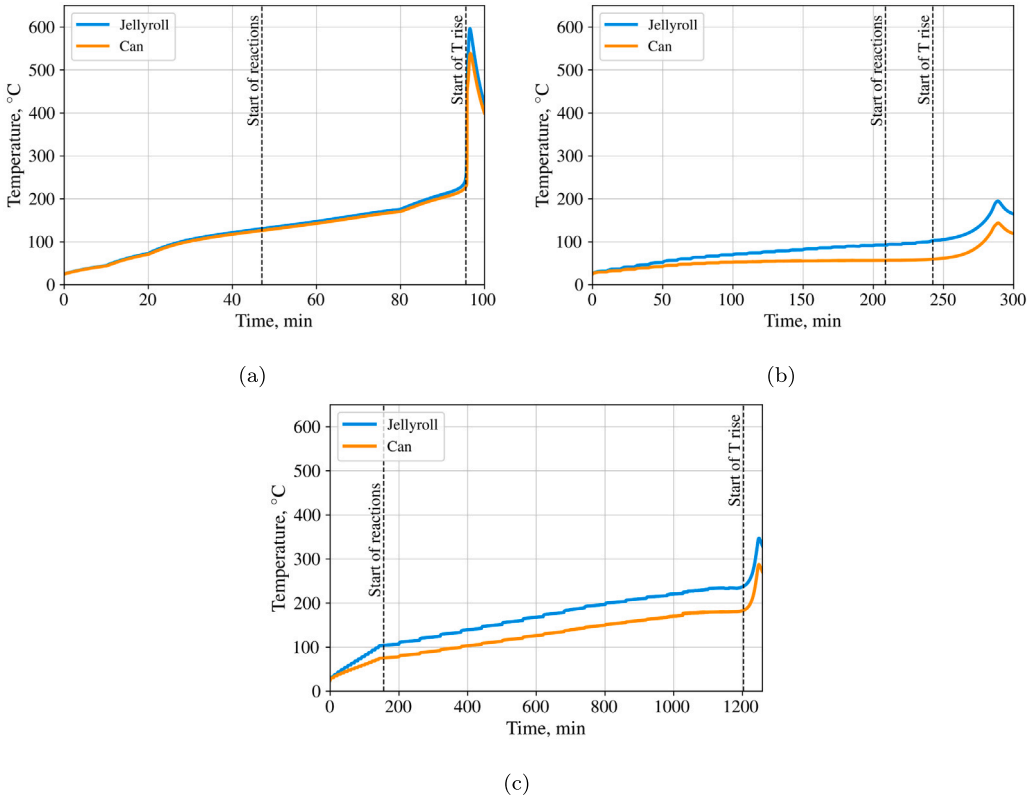

Fig. 10. Simulated temperature profiles of the external can and the jellyroll for different cooling configurations: (a) natural convection air cooling, (b) immersion cooling with low boiling temperature fluid, and (c) immersion cooling with high boiling temperature fluid.

In contrast, the IC configurations significantly improved thermal management performance. This enhancement is primarily attributed to the higher thermal capacity of the dielectric fluids and the efficient heat removal enabled by boiling heat transfer.

Between the two IC strategies, the high boiling point fluid demonstrated the highest effectiveness in delaying TR, requiring considerably greater power and energy input compared to the air-cooled case. This superior performance results from the combined effect of efficient heat transfer provided by liquid direct cooling during the initial stages of heating and the activation of phase change mechanism in the later stages, when rapid heat removal becomes essential to prevent the onset of self-sustaining reactions. As a consequence, the consumption of reactants is slower and more gradual, allowing the energy release from exothermic reactions to be better controlled. Eventually, the temperature becomes high enough that the system can no longer suppress TR, and reactions proceed until near-complete depletion of reactants. However, by that point, a substantial amount of the energy has already been dissipated and most of the reactants consumed, notably reducing the severity of the TR event.

The low boiling point fluid also outperformed air cooling, but its early boiling onset limited its overall effectiveness compared to the high boiling case. Although average temperatures remain lower, as the battery approaches TR trigger conditions, the boiling regime nears saturation and the battery surfaces become almost entirely covered by a vapor film. This vapor layer considerably reduces the ability of the system to absorb additional heat, thus facilitating the onset of TR. In this configuration, the strong thermal gradient established within the jellyroll allows the core to reach temperatures sufficient to trigger self-sustaining reactions, while the cooler outer layers hinder the outward propagation of the reaction front, partially suppressing the evolution of TR. Nonetheless, because the reactants are not fully depleted, a subsequent temperature rise could eventually lead to the re-initiation of reactions.

Additionally, it should also be emphasized that the heating procedure has a significant influence on TR dynamics, as it determines the heating rate applied to the battery. Therefore, the presented results are valid only within the context of the specific thermal scenario considered in the study. For this reason, it is worth noting that in scenarios characterized by more aggressive heating rates, the lower overall temperatures maintained by the low boiling point configuration could potentially help delay or mitigate the onset of TR. Conversely, the delayed boiling onset in the high boiling point configuration may become disadvantageous if exothermic reactions evolve irreversibly before boiling occurs, making the subsequent phase-change mechanism ineffective.

While the results clearly highlight the superior performance of IC strategies, some model assumptions and limitations must be acknowledged. In particular, the calibration of the boiling model plays a critical role. Due to the lack of specific experimental data for the high boiling point fluid, the Rohsenow correlation was calibrated using the pool boiling curve of the low boiling point fluid. Moreover, when the low boiling point fluid is employed and TR occurs, the Rohsenow correlation operates close to the limits of its natural validity range, potentially leading to an overestimation of the heat transfer.

Despite these limitations, the modeling approach is considered acceptable within the scope of the present study, as it does not compromise the comparative analysis between the different cooling strategies. Future work will aim to address these aspects through the development of a dedicated experimental setup for the characterization of dielectric fluids and performance assessment of the proposed cooling strategies.

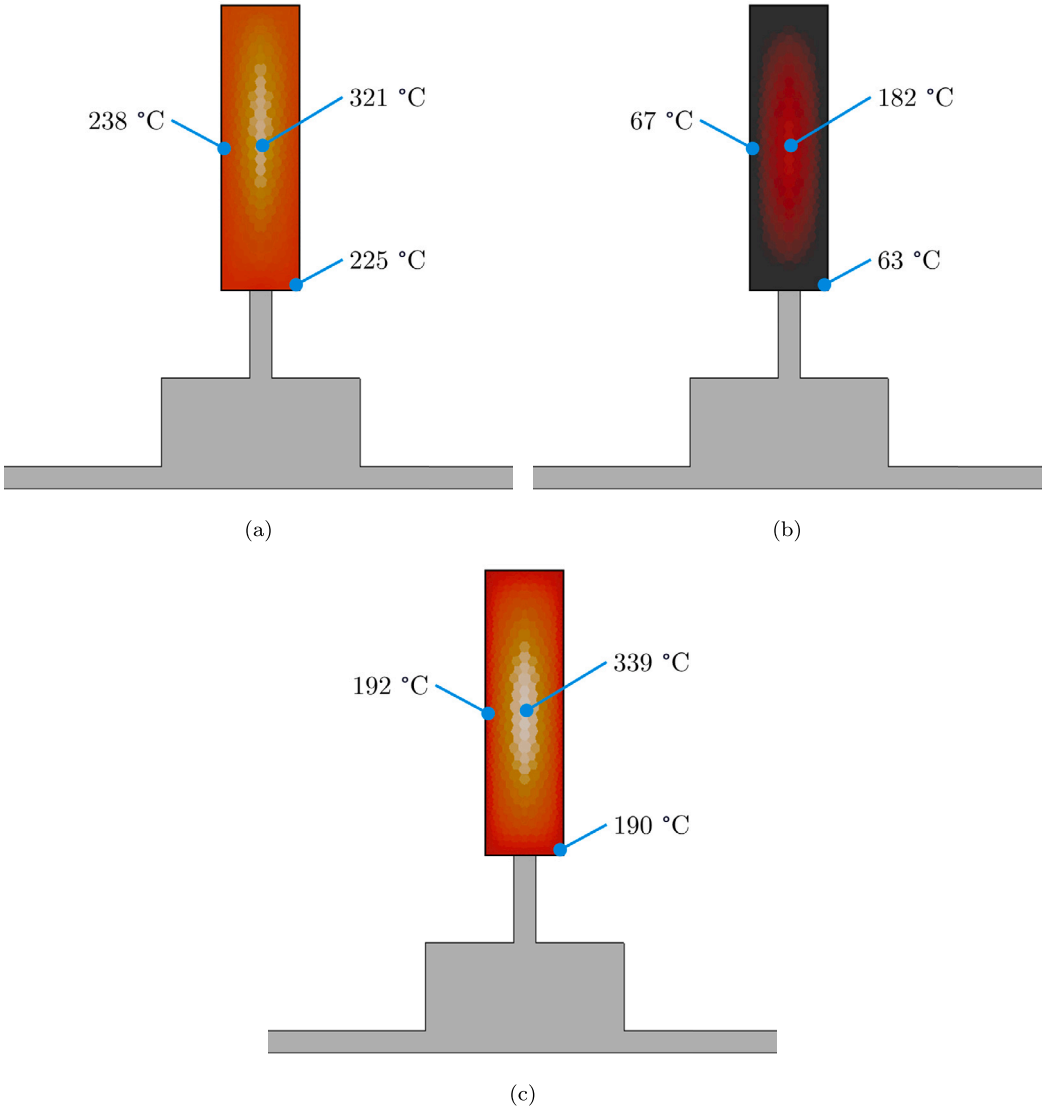

Fig. 11. Simulated temperature snapshots at the start of the steep temperature rise for different cooling configurations: (a) natural convection air cooling, (b) immersion cooling with low boiling temperature fluid, and (c) immersion cooling with high boiling temperature fluid.

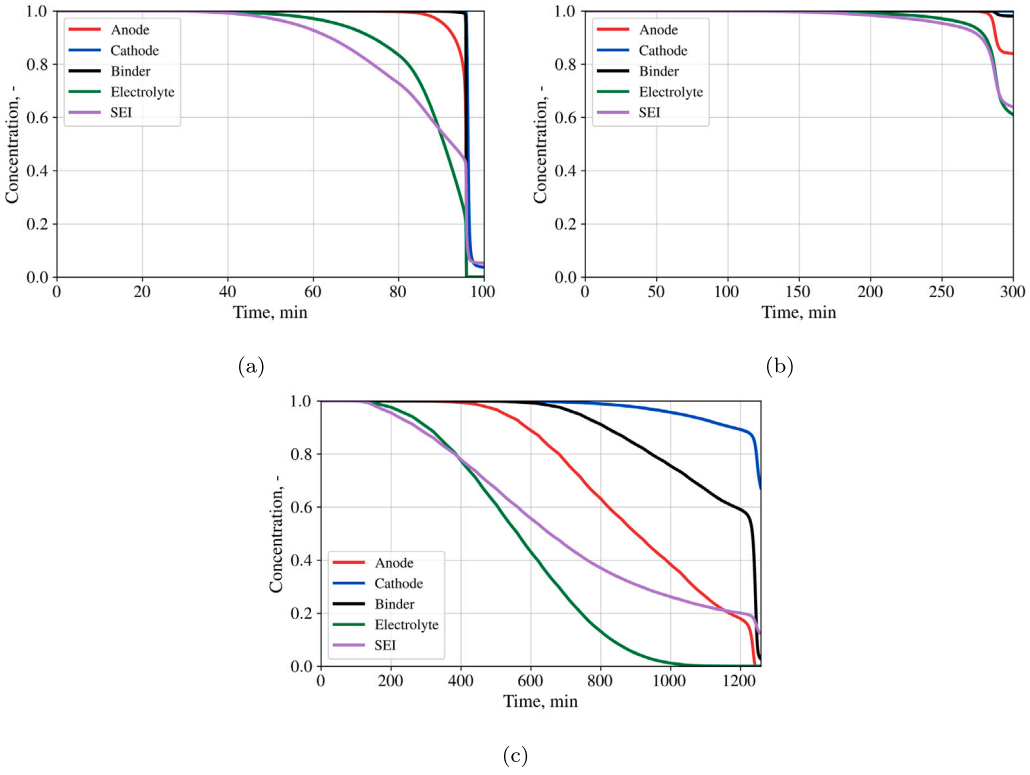

Fig. 12. Simulated concentration profiles of chemical components for different cooling configurations: (a) natural convection air cooling, (b) immersion cooling with low boiling temperature fluid, and (c) immersion cooling with high boiling temperature fluid.

Beyond modeling considerations, practical implications must also be taken into account when considering the adoption of IC systems in real-world applications, particularly in the automotive sector. The increased system complexity and additional weight represent non-negligible challenges, especially for configurations utilizing low boiling point fluids, where two-phase flow must be managed even under standard operating conditions. Nonetheless, the significant thermal management improvements and safety benefits demonstrated in this study highlight the strong potential of IC as an advanced and effective cooling solution, supporting further research and development.

CRediT authorship contribution statement

Luca Reina: Writing – original draft, Visualization, Validation, Software, Resources, Methodology, Investigation, Formal analysis, Data curation, Conceptualization. **Javier Marco-Gimeno:** Writing – review & editing, Supervision, Resources, Project administration, Conceptualization. **Carlos Micó:** Writing – review & editing, Supervision, Resources, Project administration, Conceptualization. **Stefano Fontanesi:** Writing – review & editing. **Antonio García:** Supervision, Project administration.

Declaration of competing interest

The authors declare that they have no known competing financial interests or personal relationships that could have appeared to influence the work reported in this paper.

Acknowledgments

The authors acknowledge the financial support provided by European Union, NextGenerationEU and by CNH Industrial for PhD Scholarship funding.

Data availability

Data will be made available on request.

References

[1] P. Zhang, J. Lu, K. Yang, H. Chen, Y. Huang, A 3D simulation model of thermal runaway in Li-ion batteries coupled particles ejection and jet flow, J. Power Sources 580 (2023) http://dx.doi.org/10.1016/j.jpowsour.2023.233357.

[2] D. Kong, G. Wang, P. Ping, J. Wen, A coupled conjugate heat transfer and CFD model for the thermal runaway evolution and jet fire of 18650 lithium-ion battery under thermal abuse, ETransportation 12 (2022) http://dx.doi.org/10.1016/j.etran.2022.100157.

[3] G. Wang, D. Kong, P. Ping, J. Wen, X. He, H. Zhao, X. He, R. Peng, Y. Zhang, X. Dai, Revealing particle venting of lithium-ion batteries during thermal runaway: A multi-scale model toward multiphase process, ETransportation 16 (2023) http://dx.doi.org/10.1016/j.etran.2023.100237.

[4] X. Liu, Z. Zhou, W.T. Wu, L. Wei, W. Wu, Y. Li, L. Gao, Y. Li, Y. Song, Modelling for the mitigation of lithium ion battery thermal runaway propagation by using phase change material or liquid immersion cooling, Case Stud. Therm. Eng. 52 (2023) http://dx.doi.org/10.1016/j.csite.2023.103749.

[5] J.K. Ostanek, W. Li, P.P. Mukherjee, K.R. Crompton, C. Hacker, Simulating onset and evolution of thermal runaway in Li-ion cells using a coupled thermal and venting model, Appl. Energy 268 (2020) http://dx.doi.org/10.1016/j.apenergy.2020.114972.

[6] G.H. Kim, A. Pesaran, R. Spotnitz, A three-dimensional thermal abuse model for lithium-ion cells, J. Power Sources 170 (2007) 476–489, http://dx.doi.org/10.1016/j.jpowsour.2007.04.018.

[7] D. Ren, X. Liu, X. Feng, L. Lu, M. Ouyang, J. Li, X. He, Model-based thermal runaway prediction of lithium-ion batteries from kinetics analysis of cell components, Appl. Energy 228 (2018) 633–644, http://dx.doi.org/10.1016/j.apenergy.2018.06.126.

[8] A. Kriston, I. Adanouj, V. Ruiz, A. Pfrang, Quantification and simulation of thermal decomposition reactions of Li-ion battery materials by simultaneous thermal analysis coupled with gas analysis, J. Power Sources 435 (2019) http://dx.doi.org/10.1016/j.jpowsour.2019.226774.

[9] A. Wahab, A.U.H. Najmi, H. Senobar, N. Amjady, H. Kemper, H. Khayyam, Immersion cooling innovations and critical hurdles in Li-ion battery cooling for future electric vehicles, Renew. Sustain. Energy Rev. 211 (2025) http://dx.doi.org/10.1016/j.rser.2024.115268.

[10] X. Feng, M. Ouyang, X. Liu, L. Lu, Y. Xia, X. He, Thermal runaway mechanism of lithium ion battery for electric vehicles: A review, Energy Storage Mater. 10 (2018) 246–267, http://dx.doi.org/10.1016/j.ensm.2017.05.013.

[11] C. Liu, H. Dai, D. Wang, X. Ren, S. Lyu, J. Fan, S. Lv, S. Zhu, N. Li, Y. Wang, Review—Understanding thermal runaway in lithium-ion batteries: Trigger, mechanism, and early warning strategies, J. Electrochem. Soc. 171 (2024) 120527, http://dx.doi.org/10.1149/1945-7111/ad9b9d.

[12] C. Roe, X. Feng, G. White, R. Li, H. Wang, X. Rui, C. Li, F. Zhang, V. Null, M. Parkes, Y. Patel, Y. Wang, H. Wang, M. Ouyang, G. Offer, B. Wu, Immersion cooling for lithium-ion batteries – A review, J. Power Sources 525 (2022) http://dx.doi.org/10.1016/j.jpowsour.2022.231094.

[13] X. Wu, Y. Lu, H. Ouyang, X. Ren, J. Yang, H. Guo, X. Han, C. Zhang, Y. Wu, Theoretical and experimental investigations on liquid immersion cooling battery packs for electric vehicles based on analysis of battery heat generation characteristics, Energy Convers. Manage. 310 (2024) 118478, http://dx.doi.org/10.1016/j.enconman.2024.118478, URL: https://www.sciencedirect.com/science/article/pii/S0196890424004199.

[14] A. Thiru Kumaran, S. Hemavathi, Optimization of Lithium-ion battery thermal performance using dielectric fluid immersion cooling technique, Process. Saf. Environ. Prot. 189 (2024) 768–781, http://dx.doi.org/10.1016/j.psep.2024.06.117, URL: https://www.sciencedirect.com/science/article/pii/S0957582024008024.

[15] S. Hemavathi, S. Srinivas, A. Prakash, Performance evaluation of a hydrostatic flow immersion cooling system for high-current discharge Li-ion batteries, J. Energy Storage 72 (2023) 108560, http://dx.doi.org/10.1016/j.est.2023.108560, URL: https://www.sciencedirect.com/science/article/pii/S2352152X23019576.

[16] Y. Liu, G. Aldan, X. Huang, M. Hao, Single-phase static immersion cooling for cylindrical lithium-ion battery module, Appl. Therm. Eng. 233 (2023) 121184, http://dx.doi.org/10.1016/j.applthermaleng.2023.121184, URL: https://www.sciencedirect.com/science/article/pii/S1359431123012139.

[17] J.-W. Han, K.S. Garud, E.-H. Kang, M.-Y. Lee, Numerical study on heat transfer characteristics of dielectric fluid immersion cooling with fin structures for lithium-ion batteries, Symmetry 15 (1) (2023) http://dx.doi.org/10.3390/sym15010092, URL: https://www.mdpi.com/2073-8994/15/1/92.

[18] Y. Li, Z. Zhou, L. Su, M. Bai, L. Gao, Y. Li, X. Liu, Y. Li, Y. Song, Numerical simulations for indirect and direct cooling of 54 V LiFePO4 battery pack, Energies 15 (13) (2022) http://dx.doi.org/10.3390/en15134581, URL: https://www.mdpi.com/1996-1073/15/13/4581.

[19] Y. Zhou, Z. Wang, Z. Xie, Y. Wang, Parametric investigation on the performance of a battery thermal management system with immersion cooling, Energies 15 (7) (2022) http://dx.doi.org/10.3390/en15072554, URL: https://www.mdpi.com/1996-1073/15/7/2554.

[20] M. Suresh Patil, J.-H. Seo, M.-Y. Lee, A novel dielectric fluid immersion cooling technology for Li-ion battery thermal management, Energy Convers. Manage. 229 (2021) 113715, http://dx.doi.org/10.1016/j.enconman.2020.113715, URL: https://www.sciencedirect.com/science/article/pii/S0196890420312395.

[21] H. Choi, H. Lee, J. Kim, H. Lee, Hybrid single-phase immersion cooling structure for battery thermal management under fast-charging conditions, Energy Convers. Manage. 287 (2023) 117053, http://dx.doi.org/10.1016/j.enconman.2023.117053, URL: https://www.sciencedirect.com/science/article/pii/S0196890423003990.

[22] J. Liu, Q. Ma, X. Li, Numerical study on heat dissipation performance of a lithium-ion battery module based on immersion cooling, J. Energy Storage 66 (2023) 107511, http://dx.doi.org/10.1016/j.est.2023.107511, URL: https://www.sciencedirect.com/science/article/pii/S2352152X23009088.

[23] M. Carello, M. Bovio, F. Ricci, S. Dall'acqua, D.I. Strano, A. Rizzello, CFD simulation and modelling of a battery thermal management system: Comparison between indirect and immersion cooling, SAE Int. J. Adv. Curr. Pr. Mobil. 6 (2023) http://dx.doi.org/10.4271/2023-01-0514.

[24] J. Li, J. Ou, S. Zeng, L. Chen, Y. Qiao, Z. Tan, Y. Li, W. Wu, Immersion cooling enabled thermal runaway prevention in overcharged batteries: Mechanisms and metrics, Appl. Energy 401 (2025) http://dx.doi.org/10.1016/j.apenergy.2025.126798.

[25] L. Zhao, G. Song, X. Yang, R. Pan, Experiments on the effects of liquid immersion cooling on the thermal runaway (TR) behaviors of 280 Ah lithium-ion batteries subjected to different TR-triggering conditions, J. Energy Storage 121 (2025) http://dx.doi.org/10.1016/j.est.2025.116358.

[26] W. Ke, B. Tong, W. Zhang, T. Hu, W. Gao, J. Xu, S. Li, P. Tan, Experimental comparison of static immersion cooling and natural air cooling for suppressing thermal runaway triggering in lithium-ion battery modules, J. Energy Storage 149 (2026) http://dx.doi.org/10.1016/j.est.2026.120444.

[27] S. Lei, L. Huaiyu, T. Bojun, Z. Chunfeng, Z. Xiaojun, W. Liyang, Experiments on liquid-immersed thermal runaway management for large energy-stored lithium-ion battery modules, Therm. Sci. Eng. Prog. 68 (2025) http://dx.doi.org/10.1016/j.tsep.2025.104347.

[28] 3M, 3M^{TM} Novec^{TM} 649 engineered fluid datasheet, 2009, URL: https://multimedia.3m.com/mws/media/569865O/3m-novec-engineered-fluid-649.pdf. (Accessed April 2025).

[29] 3M, 3M^{TM} Fluorinert^{TM} electronic liquid FC-43 datasheet, 2019, URL: https://multimedia.3m.com/mws/media/64889O/fluorinert-electronic-liquid-fc-43.pdf. (Accessed April 2025).

[30] Siemens Digital Industries Software, Simcenter STAR-CCM+, version 2310, 2023.

[31] R.M. Spotnitz, J. Weaver, G. Yeduvaka, D.H. Doughty, E.P. Roth, Simulation of abuse tolerance of lithium-ion battery packs, J. Power Sources 163 (2007) 1080–1086, http://dx.doi.org/10.1016/j.jpowsour.2006.10.013.

[32] T.D. Hatchard, D.D. MacNeil, A. Basu, J.R. Dahn, Thermal model of cylindrical and prismatic lithium-ion cells, J. Electrochem. Soc. 148 (2001) A755, http://dx.doi.org/10.1149/1.1377592.

[33] X. Feng, X. He, M. Ouyang, L. Lu, P. Wu, C. Kulp, S. Prasser, Thermal runaway propagation model for designing a safer battery pack with 25Ah LiNixCoyMnzO2 large format lithium ion battery, Appl. Energy 154 (2015) 74–91, http://dx.doi.org/10.1016/j.apenergy.2015.04.118.

[34] S. Bilyaz, K.C. Marr, O.A. Ezekoye, Modeling of thermal runaway propagation in a pouch cell stack, Fire Technol. 56 (2020) 2441–2466, http://dx.doi.org/10.1007/s10694-020-00970-6.

[35] N. Weber, S. Schuhmann, J. Tübke, H. Nirschl, Chemical thermal runaway modeling of lithium-ion batteries for prediction of heat and gas generation, Energy Technol. 11 (2023) http://dx.doi.org/10.1002/ente.202300565.

[36] H.E. Kissinger, Variation of peak temperature with heating rate in differential thermal analysis, J. Res. Natl. Bur. Stand. 57 (1956) http://dx.doi.org/10.6028/jres.057.026.

[37] A. García, J. Monsalve-Serrano, R.L. Sari, Á.F. Robles, Numerical analysis of kinetic mechanisms for battery thermal runaway prediction in lithium-ion batteries, Int. J. Engine Res. 23 (2022) 1691–1707, http://dx.doi.org/10.1177/14680874211029902.

[38] W.M. Rohsenow, A Method of Correlating Heat Transfer Data for Surface Boiling of Liquids, Technical Report, Massachusetts Institute of Technology, 1951, URL: http://hdl.handle.net/1721.1/61431.

[39] Siemens Digital Industries Software, Simcenter STAR-CCM+ user guide v. 2310, 2023.

[40] A.J.G. Yunus A. Çengel, Heat and Mass Transfer: Foundamentals and Applications, McGraw-Hill Education, 2014.

[41] C. Falsetti, J. Chetwynd-Chatwin, E.J. Walsh, Pool boiling heat transfer of Novec 649 on sandblasted surfaces, Int. J. Thermofluids 22 (2024) http://dx.doi.org/10.1016/j.ijft.2024.100615.

[42] R. Hohl, J. Blum, M. Buchholz, T. Lüttich, H. Auracher, W. Marquardt, Model-based experimental analysis of pool boiling heat transfer with controlled wall temperature transients, Int. J. Heat Mass Transfer 44 (12) (2001) 2225–2238, http://dx.doi.org/10.1016/S0017-9310(00)00272-6.

[43] P.T. Coman, E.C. Darcy, C.T. Veje, R.E. White, Modelling Li-Ion cell thermal runaway triggered by an internal short circuit device using an efficiency factor and arrhenius formulations, J. Electrochem. Soc. 164 (4) (2017) A587, http://dx.doi.org/10.1149/2.0341704jes.

[44] A. García, J.V. Pastor, J. Monsalve-Serrano, D. Golke, Cell-to-cell dispersion impact on zero-dimensional models for predicting thermal runaway parameters of NCA and NMC811, Applied Energy 369 (2024) http://dx.doi.org/10.1016/j.apenergy.2024.123571.